# 36A.0 MICROSTRUCTURAL EVOLUTION IN TITANIUM ALLOYS UNDER ADDITIVE MANUFACTURING CONDITIONS

Student: Alec Saville (Mines)
Faculty: Amy Clarke (Mines)
Industrial Mentor(s): Adam Pilchak (MRL), Jessica Buckner (SNL), and Andrew Kustas (SNL)

This project started in Fall 2018 and was initially supported by the Office of Naval Research. This project is currently supported by the National Science Foundation Graduate Research Fellowships Program (NSF GRFP). The research performed during this project will serve as the basis for a PhD thesis program for Alec Saville.

## 36A.1 Project Overview and Industrial Relevance

Over the last decade, metallic additive manufacturing (AM) has seen increasing use in the creation of near-net shape, functional and structural components (not safety critical). The primary benefit of AM over traditional processing is the ability to create custom geometries beyond what is possible with traditional manufacturing, and to reduce the waste associated with extensive machining [36A.1-2]. Several challenges exist in effectively employing, qualifying, and certifying AM parts, limiting metallic AM parts to low-risk applications. These include maintaining control of microstructure during the build process via careful selection of build parameters, limiting defects like porosity and cracking, controlling anisotropic loading responses, and limiting detrimental microstructural formations [36A.3-4]. The influence of processing parameters (e.g., scan strategy, power setting, etc.) on microstructure and defect development is not well-understood, and remains an active area of research.

This project focuses on evaluating how the microstructure of Ti-6Al-4V responds to changes in build parameters and processing conditions during AM, while also exploring new avenues for microstructural refinement in emerging titanium alloys designed for AM. Samples of electron beam melted powder bed fusion (EBM-PBF) Ti-6Al-4V produced with varying scan strategies and wire-arc AM (WAAM) Ti-6Al-4V from a large-volume build are being evaluated to elucidate how changes in build parameters within the same build process (e.g., scan strategy), or changes between build processes (EBM-PBF versus WAAM with significantly different length scales and processing conditions), alter microstructure development. Exploration of microstructural refinement during AM builds with other titanium alloys is also planned as part of future work.

The three samples of EBM Ti-6Al-4V evaluated here were produced at Oak Ridge National Laboratory (ORNL) with different scan strategies identified as Raster, Dehoff, and Random. Random and Dehoff are spot melt methods, melting material in spots instead of in a linear fashion (**Figure 36A.1)**. Raster is a traditional scan strategy, whereby powder is melted linearly in every layer, and the travel path is rotated 67.5° between layers (**Figure 36A.2)**. The WAAM specimens were produced at Sandia National Laboratory (SNL) in a large-bowl build geometry using argon shielding gas (**Figure 36A.3**). Future alloys for studying microstructural refinement will be custom ordered or produced on site as need be.

## 36A.2 Previous Work

### 36A.2.1 Solidification Simulations of EBM-PBF Ti-6Al-4V Builds

To evaluate the accuracy of previous $\beta$-Ti reconstructions completed on EBM-PBF Ti-6Al-4V, the solidification conditions of the three EBM Ti-6Al-4V builds were evaluated. Thermal conditions were modelled by partners at ORNL for the deposition of one layer for each scan stategy, while thermal gradient and solidification velocity were extracted at Mines. These simulated values were compared against previously generated columnar-to-equiaxed-transition (CET) solidification models for each scan strategy to determine the expected morphology and size of grains during the solidification process. These predictions were then compared to the $\beta$-Ti reconstructions (**Figure 36A.4**) and observable prior $\beta$-Ti grain sizes from SEM characterization to validate previous findings. The extracted results were overlaid on the model generated by Kobryn et al. [36A.5], and are illustrated in **Figure 36A.5** for data points at the top of a melt pool.

These findings match the reconstructed and observed $\beta$-Ti grain sizes. Simulations of the two spot scan strategies, Dehoff and Random, predict solidification conditions within the mixed equiaxed-columnar regime and at higher GxV

values than the Raster scan strategy. This is consistent with the finer as-solidified grain size and the reconstructed $\beta$-Ti orientations. It is worth noting Random exhibited finer as-soldified grains, which is additionally supported by the model, predicting a greater amount of equiaxed grains forming during solidification. Raster was predicted to be primarily within the columnar regime of solidification, consistent with the reconstructed microstructures. However, the model also predicted partial equiaxed solidification, but it is likely any such solidification product formed higher up in the melt pool and was consequently remelted upon the next layer's deposition. Thus, equiaxed solidification from the melting process was not directly observed. In contrast, finer grain sizes were obtained more frequently in solidification and often deeper in the melt pool for the spot scan strategies. Consequently, equiaxed solidification morphologies remained obvious in the as-built microstructure.

### 36A.2.2 WAAM Ti-6Al-4V Microstructural Characterization and Initial Orientation Measurements

Samples of WAAM Ti-6Al-4V acquired from SNL were sectioned and mounted for orientation assessment and microstructural characterization. Sections of these specimens were metallographically prepared using a nonstandard 200 grit, 9 μm, and 0.04 μm preparation process after encountering challenges with traditional diamond based preparation.

Initial SEM imaging demonstrated a typical microstructure for WAAM Ti-6Al-4V builds. Regions of thin, basketweave $\alpha$-Ti with limited $\beta$-Ti (**Figure 36A.6a**) were observed, along with thicker basketweave $\alpha$-Ti with increasing quantities of $\beta$-Ti (**Figure 36A.6b**). This change in size and phase fraction indicate noticeable changes in local cooling rates from the last excursion into the $\beta$-Ti regime. Local regions of small, elongated colonies (**Figure 36A.6c**) with high aspect ratios and large, thin-plate colonies (**Figure 36A.6d**) were also dispersed throughout the build volume, along with grain boundary $\alpha$-Ti, indicating regions of considerably slower solid state cooling.

These results are consistent with prior work by Kelly et al., where each layer of wire deposited material creates a tiered microstructure within a previously deposited layer [36A.6]. When a given layer is being deposited, the heat from the deposition process propagates into previously deposited layers. Regions of material at the top of the previous layer encounter the greatest thermal excursion at this point, heating into the $\beta$-Ti regime and gradually cooling as the deposition process locally finishes. This slow cooling gives rise to the high aspect ratio colony morphologies. Locations in the middle of a previous layer are subject to intermediate heating and cooling rates, thereby forming coarse basketweave $\alpha$-Ti. Material towards the bottom of the layer is subject to the fastest cooling rates, and consequently forms the finer acicular $\alpha$-Ti with reduced $\beta$-Ti phase fractions. These morphologies are not perfectly layered through the build height, due to changes in local conditions, but the overall reasoning for each morphology holds in this WAAM build.

Regions of large colonies were also found interspersed throughout the build volume and at the build edges (**Figure 36A.7**). The former was attributed to pauses in the build process, likely producing slower cooling rates at the end of operation, and the latter due to reduced overlap of the heat source during deposition. This is despite traditional logic , dictating heat transfer from the surface produces faster cooling rates.

A large crack was observed ~40 mm up the build height in the as-received specimens, spanning almost the entire width of the build geometry (**Figure 36A.8**). Parallel crack formation was also observed throughout the fractured area, with many cracks propagating without direct connection to one another or a clear boundary to travel along. These unusual features were investigated using SEM, light optical microscopy (LOM), and EBSD to identify the mechanisms for crack formation and propagation, but no clear answer was identified in the previous reporting period.

## 36A.3 Recent Work

### 36A.3.1 Publication of EBM-PBF Ti-6Al-4V Work and MAUD Tutorial

Two papers summarizing previous work on EBM-PBF Ti-6Al-4V and developing an updated tutorial for the Rietveld refinement program MAUD were published. The EBM-PBF Ti-6Al-4V work was accepted into the journal Additive Manufacturing [36A.7], and the MAUD tutorial into Integrating Materials and Manufacturing Innovation in the last reporting period [36A.8].

### 36A.3.2 Large-Scale EBSD and Neutron Diffraction of WAAM Ti-6Al-4V

Large-scale EBSD of WAAM Ti-6Al-4V was completed to relate specific orientations to microstructural features observed in the previous reporting period. This also enables the reconstruction of the as-solidified $\beta$-Ti microstructure and crystallographic texture. Neutron diffraction up the build height in ~ 10 mm intervals was also completed to assess bulk crystallographic texture as a function of build height.

Previous work on EBM-PBF Ti-6Al-4V identified specific $\alpha$-Ti orientations, which correlated to diffusional microstructures and finer as-solidified $\beta$-Ti grains [36A.7]. Neutron diffraction and EBSD on WAAM Ti-6Al-4V aims to deconvolute whether these orientations originate from finer as-solidified microstructures, or diffusional microstructures.

Neutron diffraction and EBSD scans returned the same $\alpha$-Ti textures for the WAAM samples (**Figure 36A.9**). These results indicated the presence of centimeter wide or larger parent $\beta$-Ti grains, given the restricted $\alpha$-Ti orientations observed and the high m.r.d. intensities reported. Regions towards the base of the build exhibited similar $\alpha$-Ti fiber textures to those found in the EBM-PBF Ti-6Al-4V, but these disappeared at higher build heights beyond ~ 45 mm. Reconstruction of the $\beta$-Ti phase showed large centimeter parent grains, as suggested by the $\alpha$-Ti textures. These large grains permeated the entire build height (**Figure 36A.10**), with some regions of material consisting of effectively one single $\beta$-Ti grain in width at higher build heights (**Figure 36A.11**).

With the presence of similar fiber textures in larger $\beta$-Ti grains, this work suggests previously reported microstructural → texture relationship in EBM-PBF Ti-6Al-4V originates from diffusional microstructures and not directly due to grain size. Grain size may play a role in the formation of $\alpha$-Ti fiber textures, with smaller grains reducing the diffusional distance for transformations to occur and favoring diffusional colony structures, even at higher cooling rates. Such a process would still favor the previously discovered orientations, but not directly influence their selection during transformation.

Several regions of varying parent $\beta$-Ti grain size were observed at locations where colony $\alpha + \beta$ morphologies dominated the microstructure. As seen in **Figure 36A.12**, these colony regions coincided with melt-pool like $\beta$-Ti grains and some equiaxed nucleation of $\beta$-Ti. This is theorized to originate from build pauses and restarts changing the thermal conditions for the next layer. With higher heat extraction due to a cooler build volume from the build pause, the newly deposited material favors smaller columnar grains or equiaxed solidification where heat extraction was greatest. The aforementioned colony regions are the last layers of build material deposited before a build pause. Due to the long cooling cycle before the next layer was deposited, these colonies can grow to the large observed sizes. Some colony regions are destroyed during the deposition of the next layer by remelting or re-transformation into $\beta$-Ti, but enough was sufficiently unaltered to remain a distinct region in the build volume.

Portions of the microstructure exhibiting colony microstructures and the "melt pool" $\beta$-Ti grains also exhibited the most pronounced cracking, including the near complete cracking of the specimen width at about ~ 40 mm in build height. Such cracking was theorized to originate from residual stresses in the build process aligned parallel to the build direction. The favorable crack propagation in colony microstructures was due to the colonies acting as continuous crystallographic highways, rather than the more tortuous path associated with basketweave microstructures elsewhere in the build. A Schmid factor analysis (**Figure 36A.13**) was completed to prove the crack propagation path through the colony microstructure according to literature findings [36A.9]. It is recommended build pauses not be employed in WAAM Ti-6Al-4V builds to avoid the formation of discontinuous solid-state microstructures and consequently reduce cracking formation.

### 36A.3.3 Estimating Elastic Moduli From Crystallographic Texture

In order to better inform future mechanical testing of EBM-PBF Ti-6Al-4V, an assessment of elastic modului as a function of crystallographic texture was started. A collaboration with PhD student Jeff Rossin at the University of California Santa Barbara (UCSB) was initiated to calculate the elastic moduli of each specimen produced by EBM-PBF using resonant ultrasound spectroscopy. The results from these calculations have been collected and will be used to identify orientations of interest (relative to the build direction), where mechanical testing can capture anisotropy from crystallographic texture.

### 36A.4 Plans for Next Reporting Period

Future work will focus on evaluating anisotropy from crystallographic texture via mechanical testing and RUS, publishing work on the WAAM Ti-6Al-4V microstructure, texture, and crack propagation, and evaluating other titanium alloys for additive manufacturing applications. A new collaboration with VTT-Finland on forward modelling the mechanical properties of AM microstructures, crystallographic texture, and completing crystal plasticity simulations is also starting, employing the EBM-PBF Ti-6Al-4V data reported upon previously.

### 36A.5 References

[36A.1] B. Dutta, F.H. (Sam) Froes, The Additive Manufacturing (AM) of titanium alloys, Metal Powder Report. 72 (2017) 96–106.

[36A.2] W. Frazier, Metal Additive Manufacturing: A Review, (2014).

[36A.3] S.S. Al-Bermani, M.L. Blackmore, W. Zhang, I. Todd, The Origin of Microstructural Diversity, Texture, and Mechanical Properties in Electron Beam Melted Ti-6Al-4V, Metallurgical and Materials Transactions A. 41 (2010) 3422–3434.

[36A.4] C.A. Brice, W.A. Tayon, A.L. Pilchak, Texture Development in Titanium Components Made by Additive Manufacturing, San Diego. (2014) 16.

[36A.5] Kobryn, P.A., Semiatin, S.L., 2003. Microstructure and texture evolution during solidification processing of Ti–6Al–4V. Journal of Materials Processing Technology 135, 330–339.

[36A.6] Kelly, S.M., Kampe, S.L., 2004. Microstructural evolution in laser-deposited multilayer Ti-6Al-4V builds: Part I. Microstructural characterization. Metall and Mat Trans A 35, 1861–1867.

[36A.7] Saville, A.I., Vogel, S.C., Creuziger, A., Benzing, J.T., Pilchak, A.L., Nandwana, P., Klemm-Toole, J., Clarke, K.D., Semiatin, S.L., Clarke, A.J., 2021. Texture evolution as a function of scan strategy and build height in electron beam melted Ti-6Al-4V. Additive Manufacturing 46, 102118.

[36A.8] Saville, A.I., Creuziger, A., Mitchell, E.B., Vogel, S.C., Benzing, J.T., Klemm-Toole, J., Clarke, K.D., Clarke, A.J., 2021. MAUD Rietveld Refinement Software for Neutron Diffraction Texture Studies of Single- and Dual-Phase Materials. Integr Mater Manuf Innov 10, 461–487.

[36A.9] Xie, Y., Gong, M., Luo, Z., Li, Q., Gao, M., Wang, F., Zeng, X., Wang, G., 2021. Effect of microstructure on short fatigue crack growth of wire arc additive manufactured Ti-6Al-4V. Materials Characterization 177, 111183.

### 36A.6 Figures and Tables

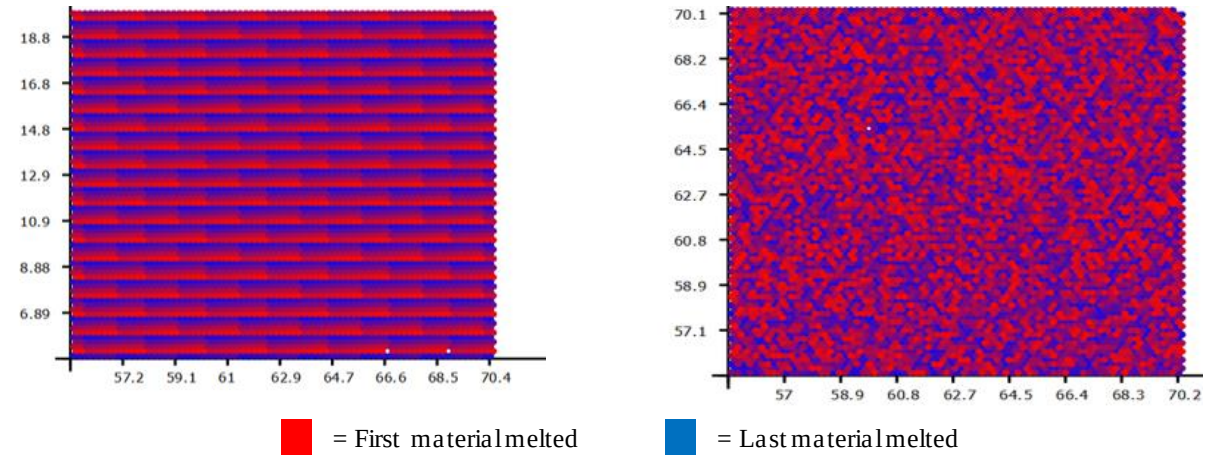


Figure 36A.1: Illustrations of the spot melt scan strategies Dehoff (left) and Random (right).

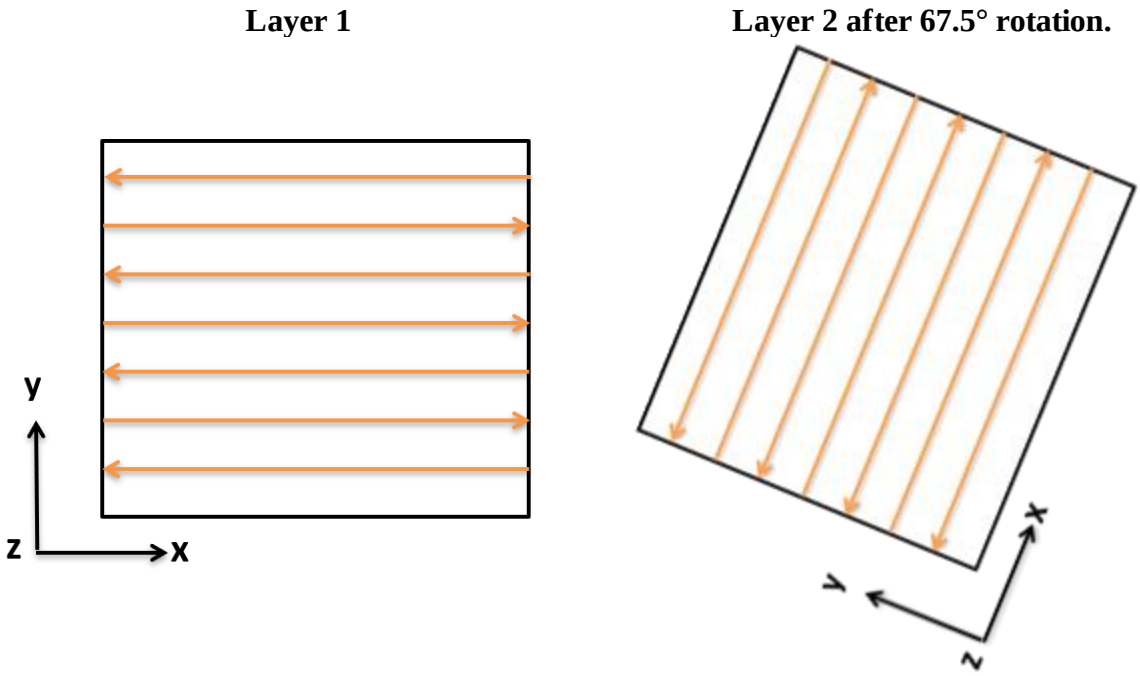


Figure 36A.2: Illustration of the Raster scan strategy. Note the 67.5° rotation between layers incorporated into this build process (right).

Figure 36A.3: Full build volume WAAM Ti-6Al-4V samples were extracted for characterization (courtesy of SNL). Samples were extracted from the two cut out sections via wire EDM.

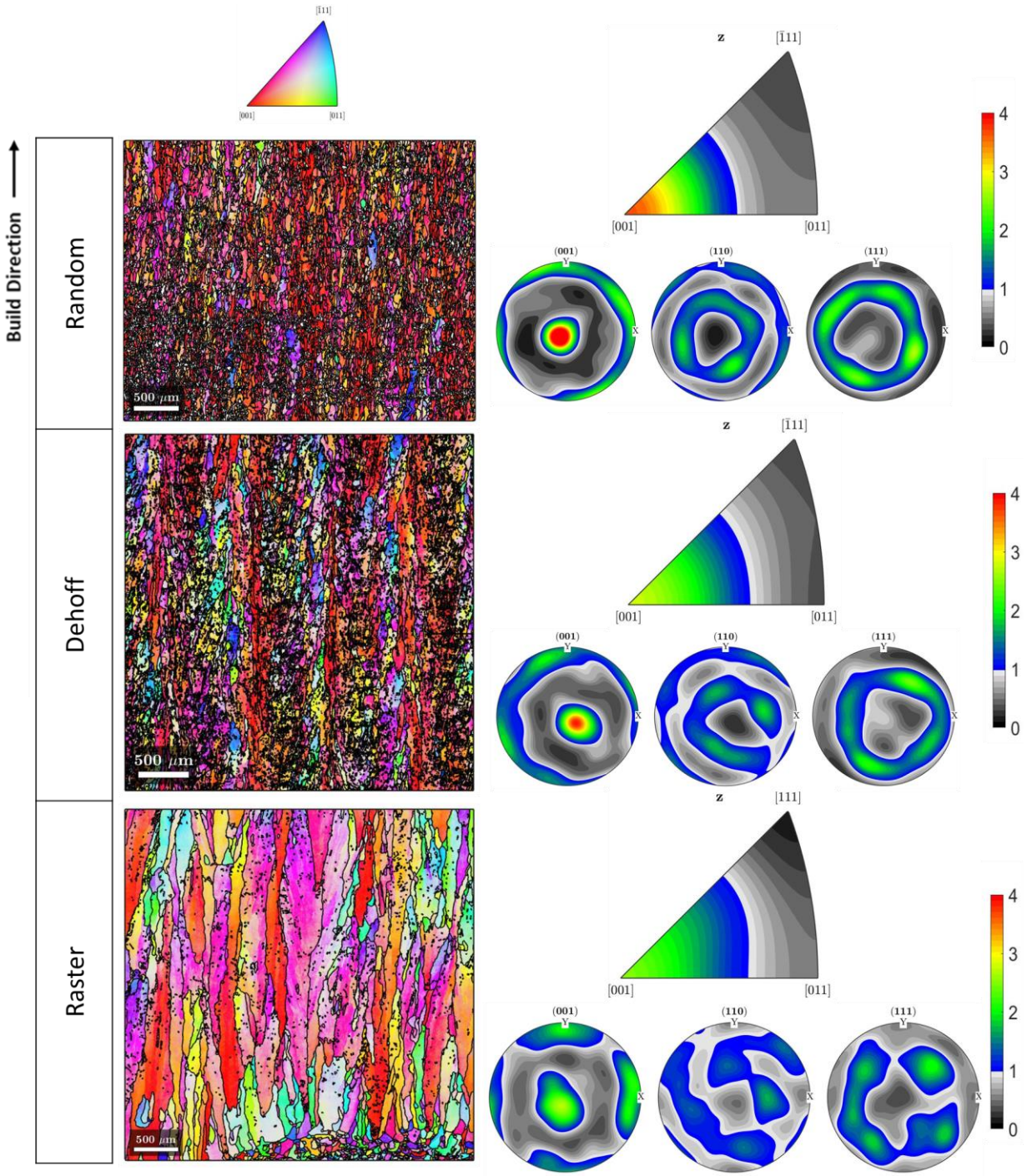


Figure 36A.4: Reconstructed $\beta$-Ti IPF maps, pole figures, and inverse pole figures for the Random (top), Dehoff (middle), and Raster (bottom) scan strategies. Note the clear difference in as-solidified grain sizes between the spot and Raster scan melt strategies, along with a change from a {001} fiber texture to a cube texture for the spot and raster melt scan strategies, respectively. All maps are colorized with respect to the build direction.

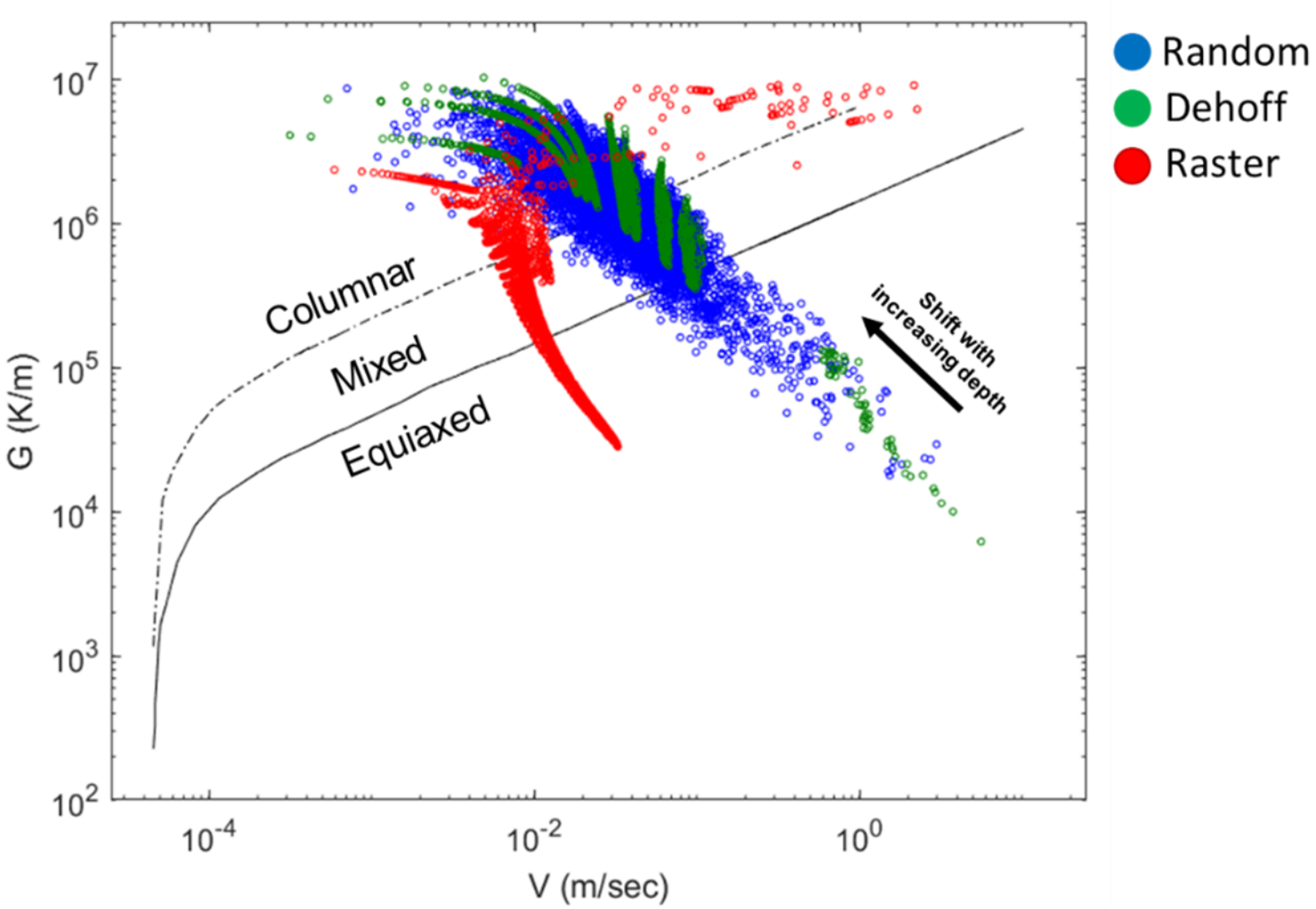


Figure 36A.5: Simulated thermal gradient (G) and solidification velocity (V) data points for the EBM Ti-6Al-4V scan strategies overlayed on a previously generated CET Ti-6Al-4V model [36.5]. Note the increased tendency for the two spot scan strategies, Dehoff and Random, to form mixed or equiaxed grains during solidification.

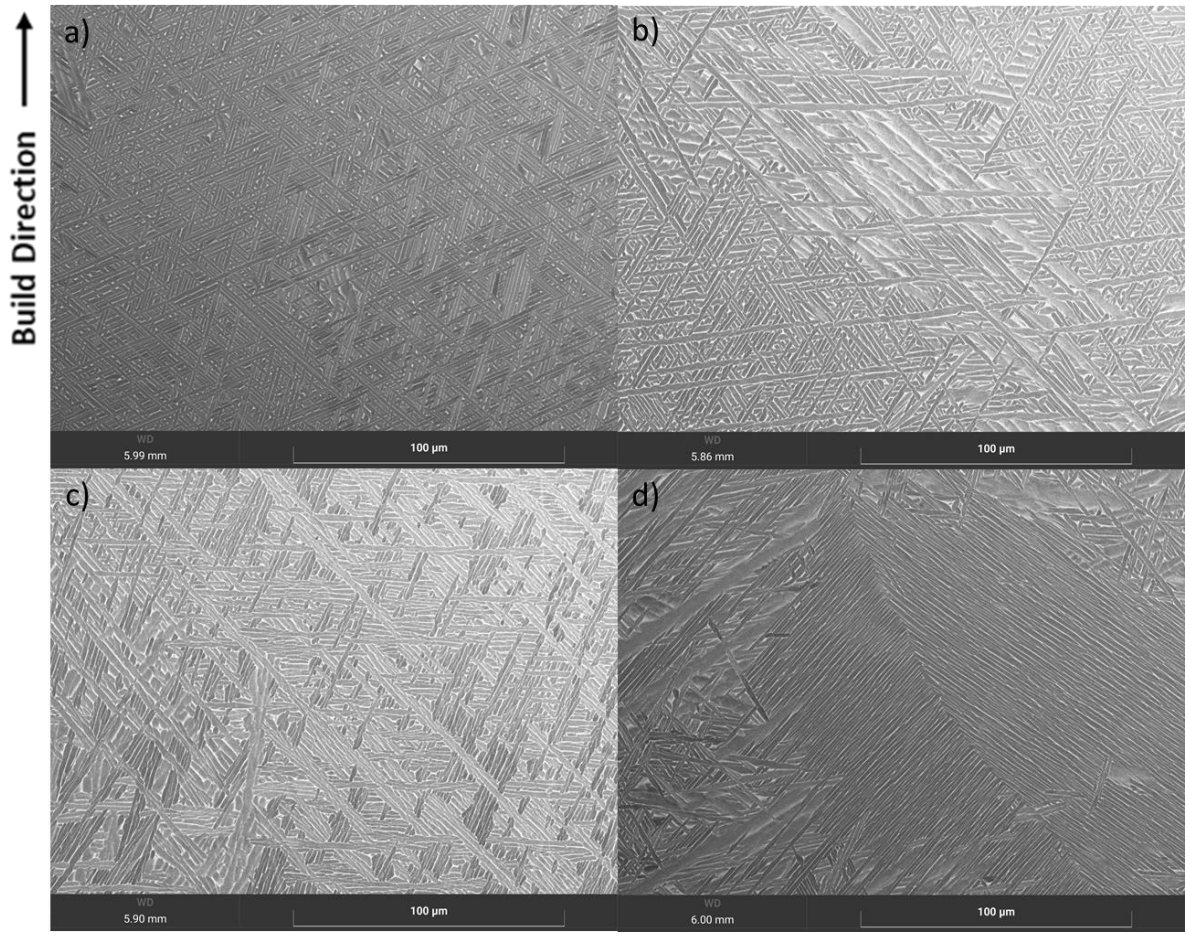


Figure 36A.6: Backscatter electron scanning electron images of the WAAM Ti-6Al-4V build, depicting fine basketweave (a), coarser basketweave (b), small elongated colonies (c), and large thin plate colonies (d).

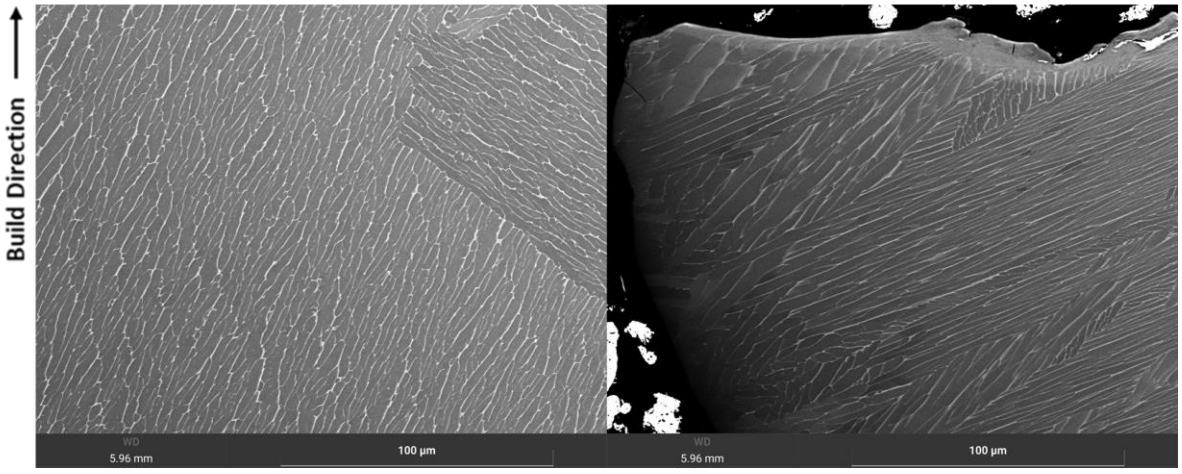


Figure 36A.7: Backscatter electron scanning electron images of the WAAM Ti-6Al-4V build, depicting large colony structures (~250 um in width) observed within the build (left) and along the build edge (right).

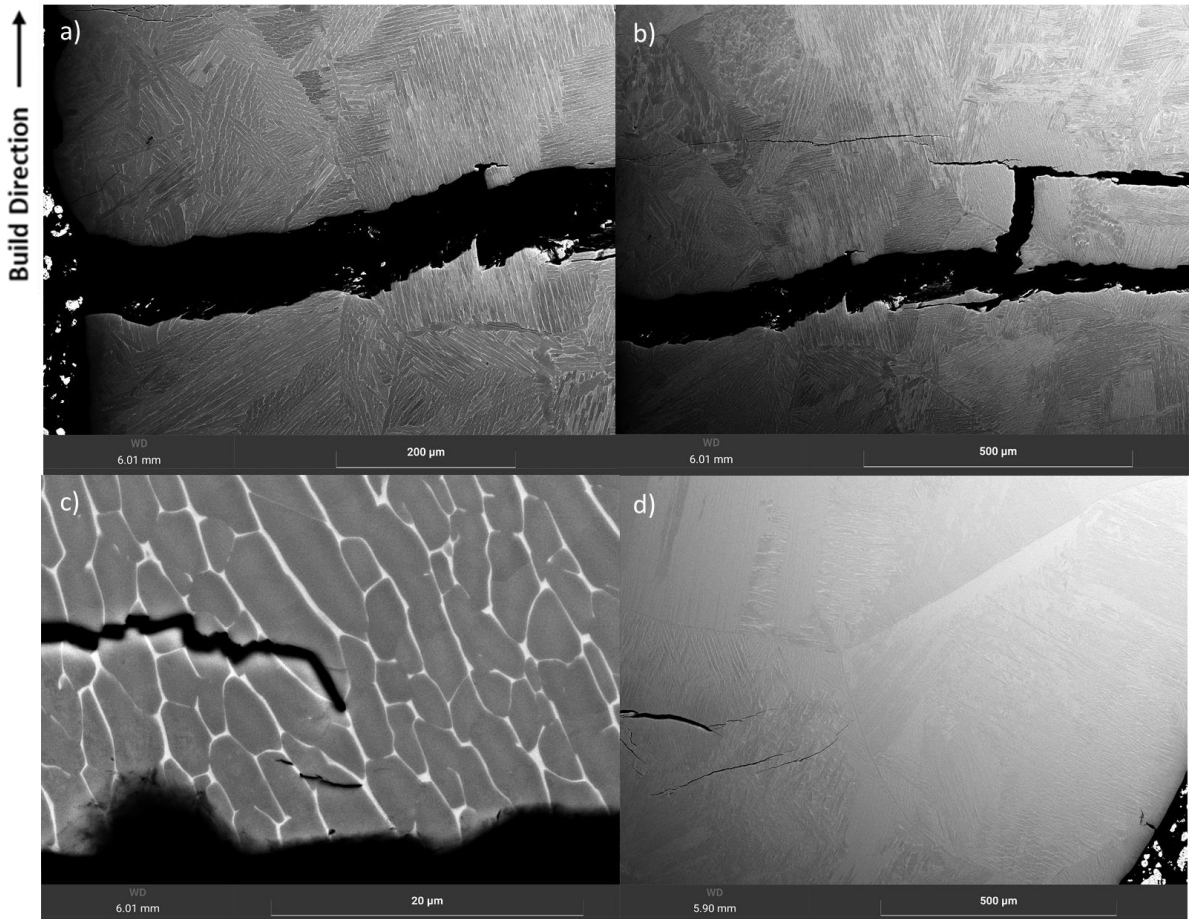


Figure 36A.8: Backscattter electron images of the crack propagation path at ~ 30 mm of the build height depicting a) the crack initiation site on the outer build surface and demonstrating no traversal of the prior $\beta$-Ti grain boundaries, b) continued propagation of the crack across colony structures and into two different crack paths, c) parallel and non-connecting crack propagation parallel to the main fracture, and d) the end of the crack path ~ 1 mm from the inner edge of the specimen width.

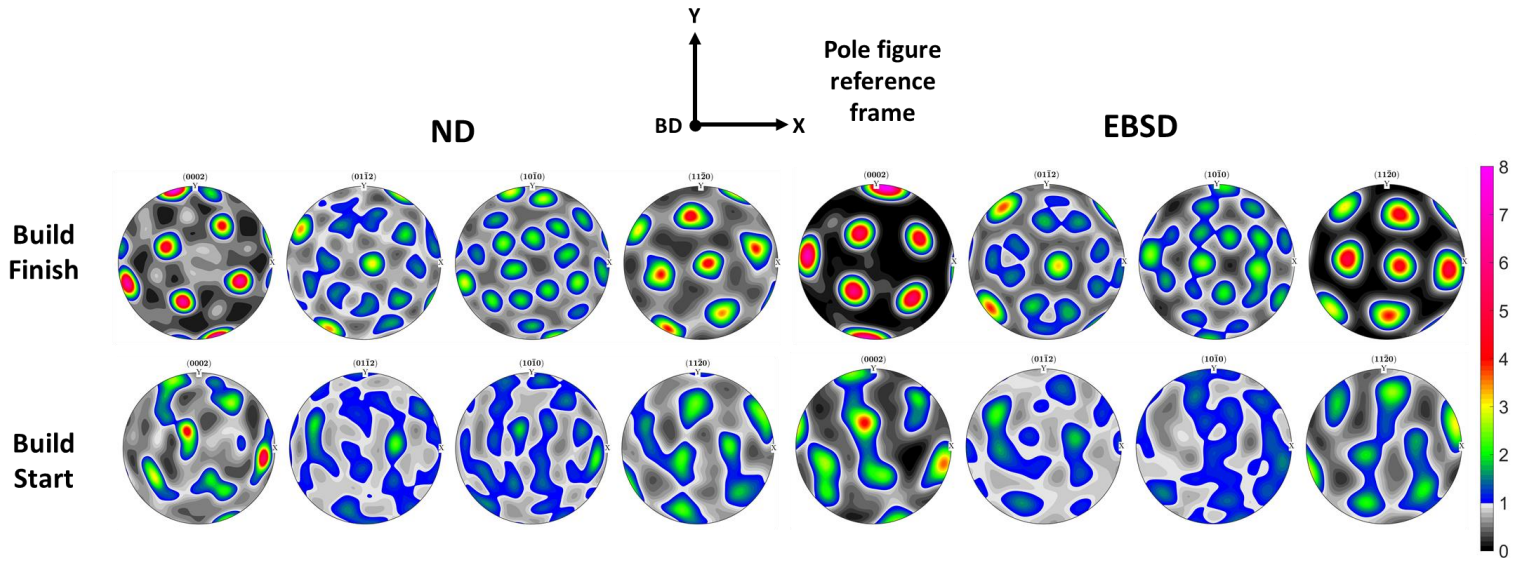


Figure 36A.9: Neutron diffraction (left) and EBSD (right) $\alpha$-Ti pole figures as a function of build height for WAAM Ti-6Al-4V. Both EBSD and neutron diffraction detected weak fiber textures towards the beginning of the build, indicating a greater concentration of diffusional microstructures and rotated cubic orientations during solidification in these regions. Both techniques also observed concentrated $\alpha$-Ti orientations at higher build heights, indicative of few $\beta$-Ti parent grains being present to produce such concentrated product orientations.

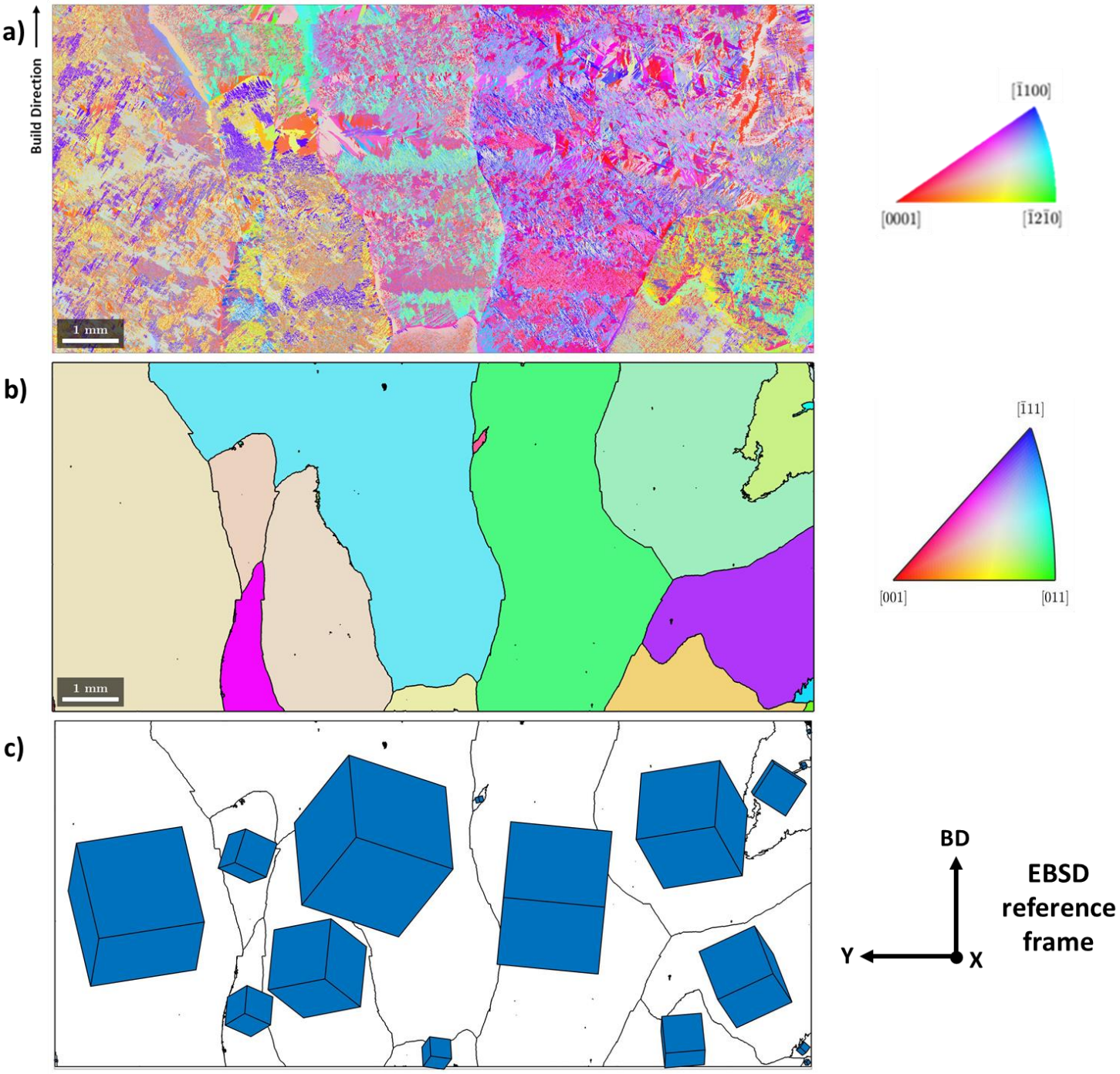


Figure 36A.10: Large-scale EBSD orientation maps for WAAM Ti-6Al-4V at ~ 15 mm in build height. $\alpha$-Ti orientation EBSD (a) demonstrated a predominantly basketweave microstructure with clear Widmanstätten banding from each consecutive layer deposition. $\beta$-Ti reconstruction (b) of the as-solidified microstructure identifies the parent grain structure clearly observed in the $\alpha$-Ti EBSD mapping. Overlaying the crystallographic orientation of each $\beta$-Ti grain was completed to more effectively demonstrate the solidification direction of the parent grains (c). All maps are colored with respect to the build direction.

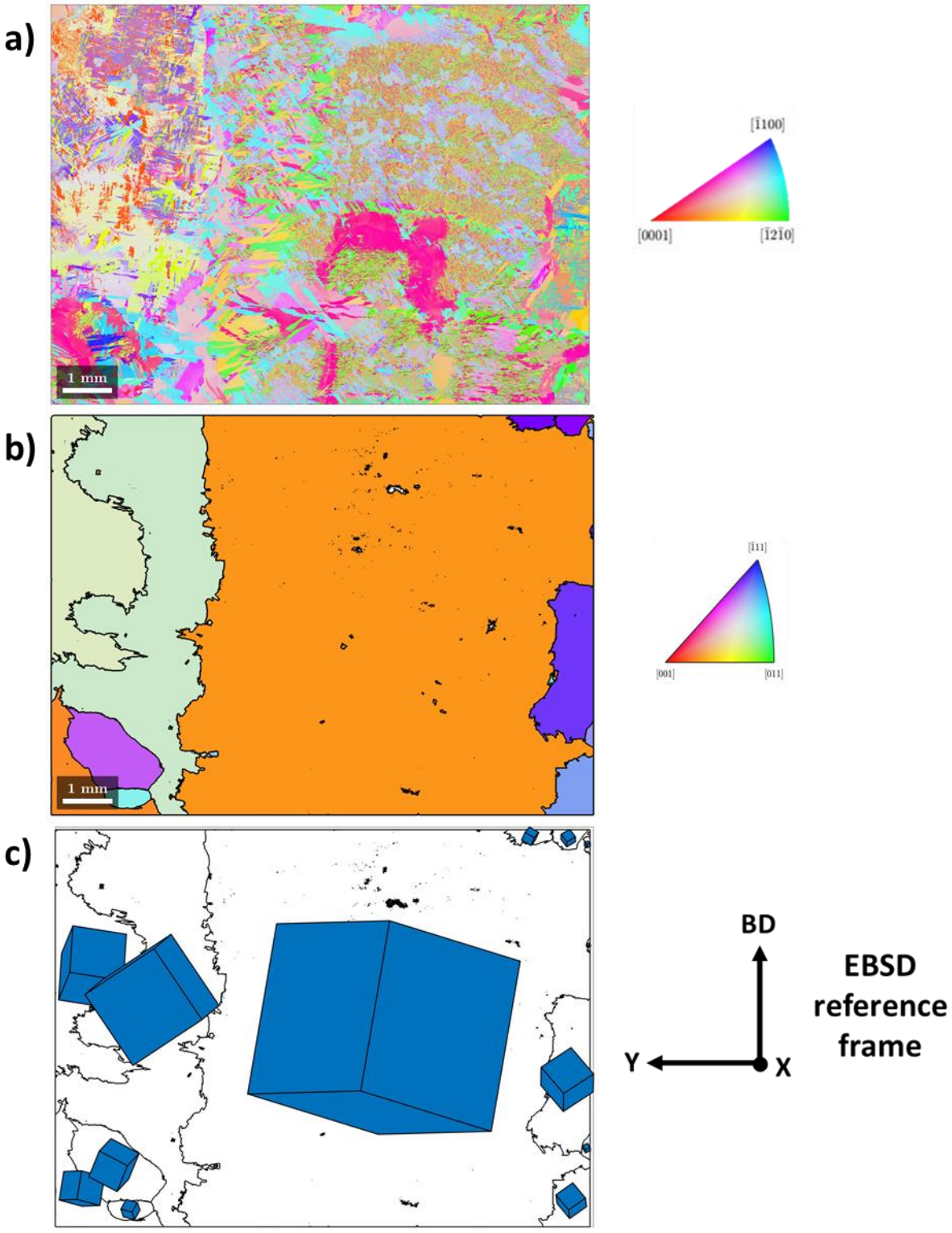


Figure 36A.11: Large-scale EBSD orientation maps for WAAM Ti-6Al-4V near the build finish and covering the effective width of the specimen. $\alpha$-Ti orientation EBSD (a) again demonstrated a predominantly basketweave microstructure with Widmanstätten banding with each newly deposited layer. $\beta$-Ti reconstruction (b) revealed the majority of this specimen's width was made of one $\beta$-Ti grain during solidification and explains the highly textured

$\alpha$-Ti orientations observed here. Overlaying the crystallographic orientation of each $\beta$-Ti grain illustrates the largest parent grain exhibited a rotated cube texture along the build direction, again explaining the $\alpha$-Ti orientations seen in EBSD and neutron diffraction. All maps are colored with respect to the build direction.

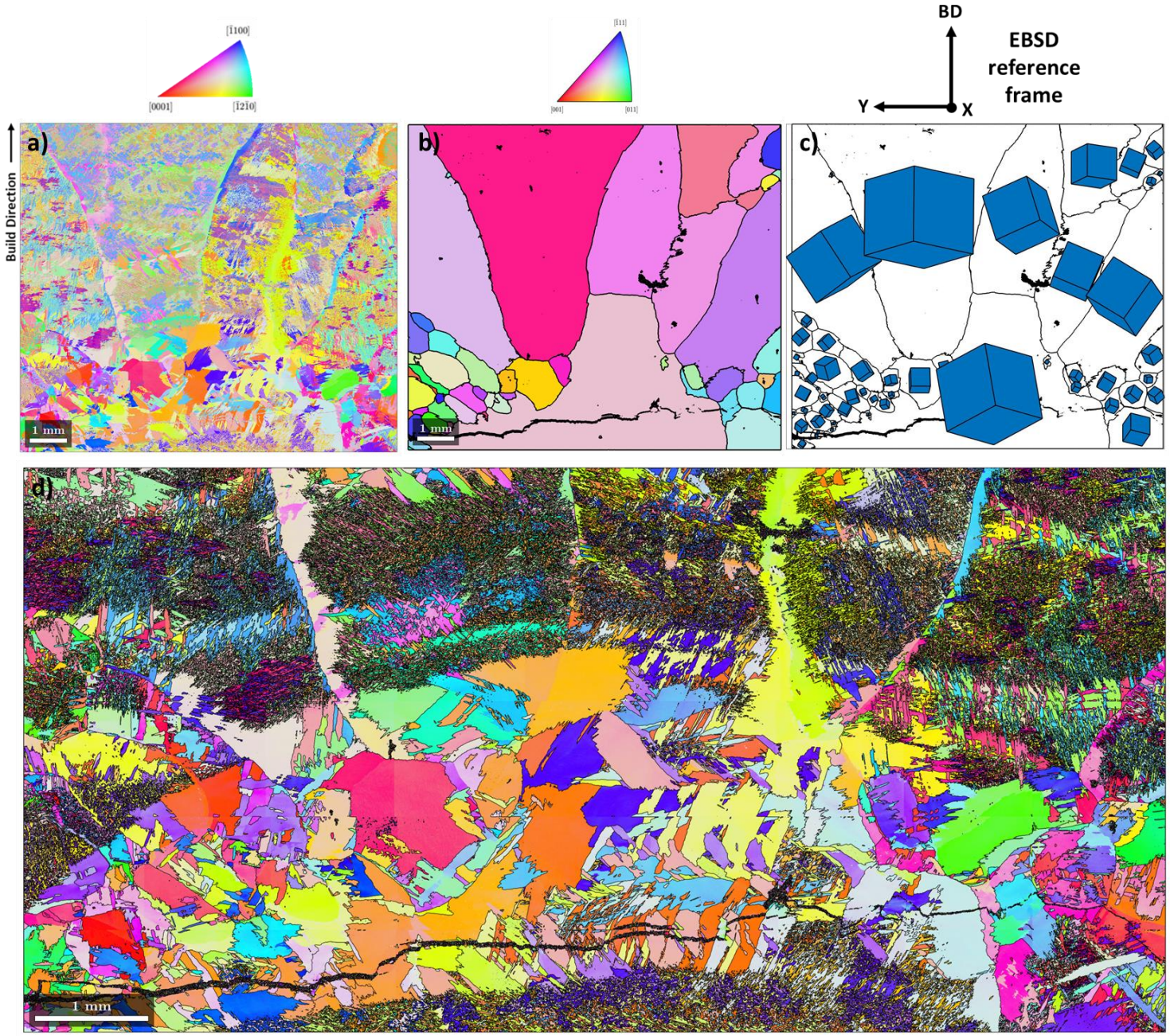


Figure 36A.12: Large-scale EBSD orientation maps for WAAM Ti-6Al-4V in a colony dominated region exhibiting significant cracking. $\alpha$-Ti orientation mapping (a) demonstrated basketeave morphology in the top half of the surveyed area where large $\beta$-Ti grains can be observed, and a colony microstructure towards the bottom portion. $\beta$-Ti reconstruction (b) demonstrated as-solidified grain geometries similar to a weld melt pool, bringing to light regions of equiaxed solidification and tilted columnar $\beta$-Ti grains. Overlaying crystal direction (c) demonstrates a clear directionality of the crystal structure to the grain growth direction, again reinforcing the theory this portion of material was subject to a lengthy pause and build restart. A finer EBSD survey of the cracked region (d) highlights the colony

dominated region, and also outlines the crack propagation path more clearly. All maps colored with respect to the build direction.

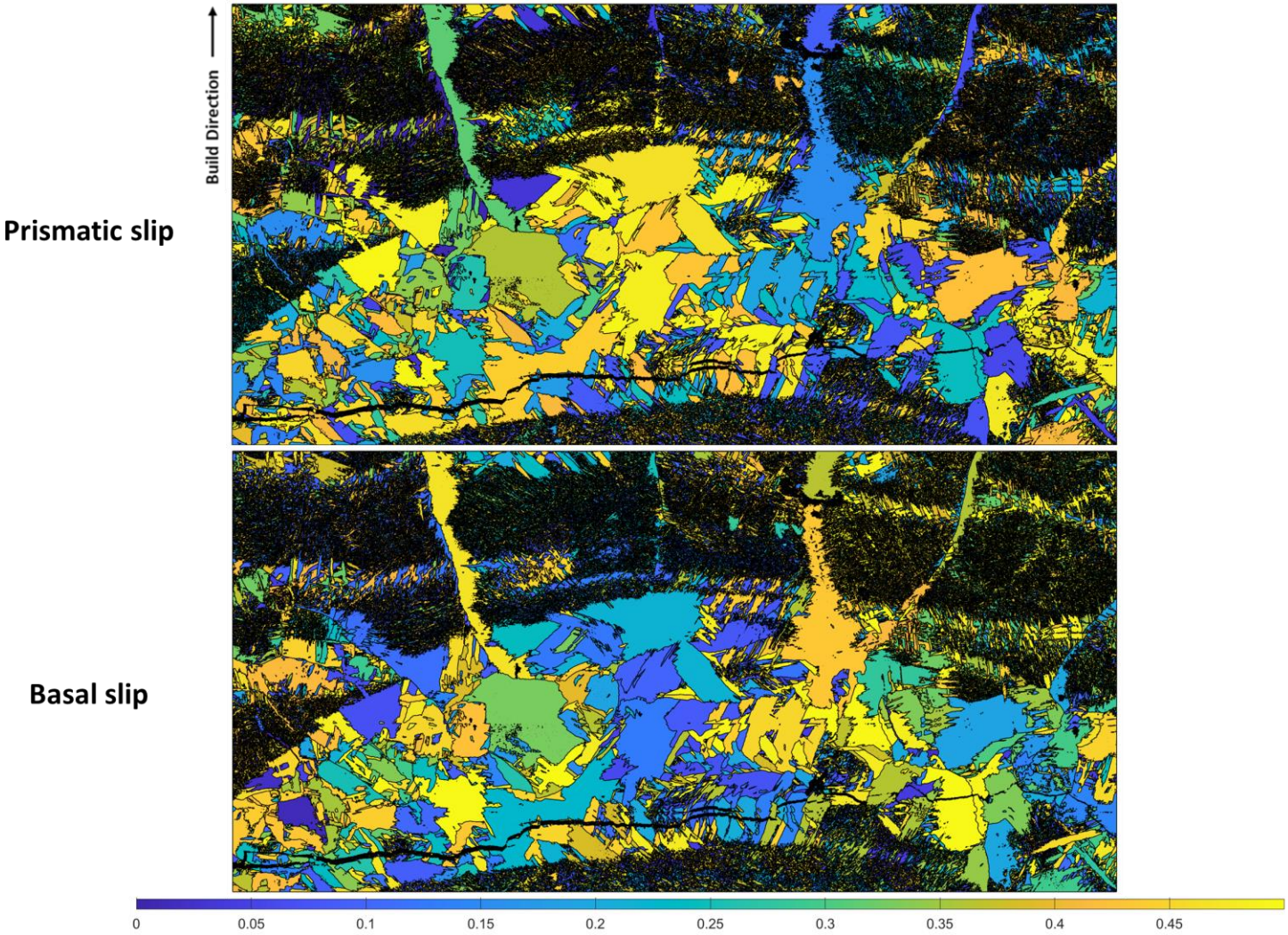


Figure 36A.13: Schmid factor maps of the cracked $\alpha + \beta$ colony region evaluated assuming a residual build stress aligned parallel to the build direction. The crack propagation in the colony microstructure was driven by whether prismatic and basal slip was more favorably aligned to the residual stress loading. Regions where neither slip system was preferentially aligned were found in some portions of the microstructure and corresponded to a more tortuous cracking path.